

# Rehabilitating C IV-based black hole mass estimates in quasars

Jessie C. Runnoe<sup>1\*</sup>, M. S. Brotherton<sup>1</sup>, Zhaohui Shang<sup>2</sup>, and M. A. DiPompeo<sup>1</sup>

<sup>1</sup>*Department of Physics and Astronomy, University of Wyoming, Laramie, WY 82071, USA*

<sup>2</sup>*Department of Physics, Tianjin Normal University, Tianjin 300387, China*

Preprint 2012 May 30

## ABSTRACT

Currently, the ability to produce black hole mass estimates using the C IV  $\lambda 1549$  line that are consistent with H  $\beta$  mass estimates is uncertain, due in large part to disagreement between velocity line width measurements for the two lines. This discrepancy between H  $\beta$  and C IV arises from the fact that both line profiles are treated the same way in single-epoch scaling relationships based on the assumption that the broad-line region is virialized, even though a non-virialized emission component is often significant in the C IV line and absent or weak in the H  $\beta$  line. Using quasi-simultaneous optical and ultra-violet spectra for a sample of 85 optically bright quasars with redshifts in the range  $z = 0.03 - 1.4$ , we present a significant step along the path to rehabilitating the C IV line for black hole mass estimates. We show that the residuals of velocity line width between C IV and H  $\beta$  are significantly correlated with the peak flux ratio of Si IV+O IV]  $\lambda 1400$  to C IV. Using this relationship, we develop a prescription for estimating black hole masses from the ultra-violet spectrum that agree better with H  $\beta$ -based masses than the traditional C IV masses. The scatter between H  $\beta$  and C IV masses is initially 0.43 dex in our sample and is reduced to 0.33 dex when using our prescription. The peak flux ratio of Si IV+O IV]  $\lambda 1400$  to C IV is an ultraviolet indicator of the suite of spectral properties commonly known as “Eigenvector 1”, thus the reduction in scatter between C IV and H  $\beta$  black hole masses is essentially due to removing an Eigenvector 1 bias in C IV-based masses.

**Key words:** galaxies: active quasars: general accretion, accretion discs black hole physics.

## 1 INTRODUCTION

Accretion onto a central supermassive black hole is the engine that powers quasars, making the black hole mass a fundamental property of the quasar. As such, the ability to make accurate measurements of black hole mass is critical for studies of active galactic nuclei (AGN). There are methods for estimating black hole mass, (see Shen 2013, for a review), but the uncertainties are large and there is room for improvement.

In current practice, black hole masses can be estimated for large numbers of AGN with single-epoch spectra using the black hole mass scaling relationships (e.g., Vestergaard & Peterson 2006). The scaling relationships take measures of velocity of gas in the broad line region (BLR) and distance from the black hole and return a virial mass under the assumption that the BLR motions in the vicinity of the black hole are dominated by its gravity. The

$R-L$  relationship (e.g., Kaspi et al. 2000; Bentz et al. 2009), a reverberation mapping result, allows the use of an easily observed continuum luminosity as a proxy for radius and velocity is taken from the line width of Doppler-broadened emission lines. Commonly used line widths include full-width at half maximum (FWHM) and line dispersion ( $\sigma_l$ ), each with their own strengths and weaknesses (Denney et al. 2009, 2013).

The scaling relationships have been calibrated for multiple emission lines, including H  $\beta$  and C IV  $\lambda 1549$  among others. The best calibration is for the H  $\beta$  line because it is the basis for the majority of reverberation mapping programs. However, at redshifts above  $z = 1.4$ , H  $\beta$  moves out of the optical wavelength window and the C IV line is more easily obtained. The reverberation mapping for C IV is more limited but does establish an  $R - L$  relationship for C IV which seems to be consistent with the results from H  $\beta$  reverberation mapping (e.g., Peterson et al. 2005). As a result, there exists a C IV-based single-epoch mass scaling relation-

\* E-mail: jrunnoe@uwyo.edu

ship that should yield mass estimates consistent with those derived from  $H\beta$ .

The reliability of the C IV line to reproduce the more trusted  $H\beta$ -based black hole mass estimates is not well established. The main criticism is that the single-epoch C IV profiles do not generally represent the reverberating BLR that provides the basis for virial mass estimates. This issue manifests itself in several specific issues that limit the successful use of C IV as a virial black hole mass estimator.

Many studies find very poor agreement and significant scatter between C IV and  $H\beta$  velocity line widths (e.g., Shen & Liu 2012). Reverberation mapping results and virial arguments suggest that the C IV emission originates in a region nearer the central black hole than does the  $H\beta$  emission (Peterson et al. 2004). This would imply that C IV line width measurements should yield broader widths than are measured for  $H\beta$ , however the C IV lines widths are often narrower than those of  $H\beta$  (e.g. Baskin & Laor 2005; Shang et al. 2007; Trakhtenbrot & Netzer 2012). Although their velocity line widths are not expected to be equal, if C IV and  $H\beta$  are both emitted from the BLR they are expected to be correlated. The fact that they are not suggests that the C IV line width measurements are not probing the velocity of the virialized C IV gas.

Line width measurements may fail to accurately reflect the velocity of the virialized gas because of contamination from other C IV-emitting regions. In regular, Type 1 AGN, the C IV line profile is often shifted from the systematic redshift of the object (Richards et al. 2002; Baskin & Laor 2005; Ho et al. 2012). This implies that the C IV-emitting gas may not be virialized as there may be a strong wind component to the gas. However, Vestergaard & Peterson (2006) find that this issue is exacerbated by including narrow-line Seyfert 1 sources, low-quality data, absorbed objects, and objects where the C IV narrow-line component is uncertain in the Baskin & Laor (2005) sample, so this issue may be less significant than it appears.

Reverberation mapping results provide another indication that line width measurements of single-epoch spectra may not reflect the velocity of virialized gas in the BLR. Denney (2012) is able to decompose the C IV emission line into a reverberating component and a non-reverberating component by comparing mean spectra, which emulate single-epoch spectra, to rms spectra, which show the emission from gas that responds to changes in the continuum, for objects with reverberation mapping coverage. The non-reverberating component contributes a fairly narrow core to the C IV line that draws the FWHM to lower values. A measure of line width in a single-epoch spectrum that might be used in a black hole mass scaling relationship is unable to separate this component from the virialized emission. Denney et al. (2009) has simulated the effects of including a non-virialized narrow component in the line widths used for black hole mass calculations. The results are conclusive: to obtain accurate and precise line width estimates, particularly when using FWHM, such contamination must be removed.

The narrow core component is much less significant in  $H\beta$  than in C IV, introducing scatter between  $H\beta$  and C IV-based black hole mass estimates. Denney (2012) recommends the shape parameter,  $S = \text{FWHM}/\sigma_1$ , for distinguishing between objects with boxy profiles ( $S \sim 1.5$ ),

indicative of a strong reverberating component, and peaky ( $S \sim 0.5$ ) profiles, indicative of a strong non-reverberating component. Furthermore, she provides a prescription for using the shape parameter to remove the bias in C IV black hole mass estimates. The shape parameter depends on C IV FWHM, and is a clear source of scatter between  $H\beta$  and C IV black hole masses.

The shape parameter, which can be used to isolate the component of the C IV emission line that originates in virialized gas and improve the reliability of C IV black hole mass estimates, is actually one among many correlated spectral properties collectively termed ‘‘Eigenvector 1’’ (EV1). EV1 describes the largest amount of variation between quasar spectra (Boroson & Green 1992), and is dominated by the anti-correlation of optical Fe II and [O III]  $\lambda 5007$  emission, with objects on one end having strong Fe II emission and weak [O III] emission. Originally defined at rest-frame optical wavelengths, EV1 has ultra-violet (UV) indicators (Brotherton & Francis 1999; Shang et al. 2003; Sulentic et al. 2007). There have been suggestions for physical drivers of EV1, including the Eddington ratio at low redshifts (Boroson & Green 1992), but it is not clear if this is the case and whether it holds at higher redshifts (Yuan & Wills 2003). Although the exact relationship between EV1 and black hole mass remains elusive, black hole mass is not the primary driver of EV1. Objects with similar black hole masses exhibit a range of EV1 properties as demonstrated in figure 6 of Boroson (2002) and therefore, crucially for this work, an object’s location on EV1 is not indicative of its intrinsic black hole mass. In some samples (e.g., the Palomar-Green sample) EV1 and black hole mass appear to be correlated but this may be the result of the sample selection and other primary correlations like the one between EV1 and Eddington fraction.

The spectral analysis of Wills et al. (1993a) suggests that it is in fact an EV1 bias that causes disagreement between the C IV and  $H\beta$  velocity widths. Their UV spectral composites demonstrate that with increasing C IV FWHM, the peak flux of the C IV line decreases compared to the peak flux of the nearby Si IV+O IV] blend at 1400 Å (which does not vary with the FWHM of C IV, Wills et al. 1993a; Richards et al. 2002) and the line profile profile changes from peaky to boxy. As a result, the velocity width of the C IV emission line is determined both by the the black hole mass and the unknown physical driver of EV1. The shape of C IV is a UV indicator of EV1, suggesting that the shape correction of Denney (2012) is successful largely because of its ability to estimate the EV1 bias in C IV. However, line dispersion, and thus the shape parameter, requires high signal-to-noise spectra to obtain an accurate measurement and is thus not suitable for use with current survey-quality data (Denney et al. 2013). Instead, the application of a peak ratio of Si IV+O IV] to C IV, a UV EV1 indicator that is free of the S/N constraint that plagues the shape parameter, combined with C IV FWHM-based black hole mass estimates might provide a more  $H\beta$ -like black hole mass that can be measured for large numbers of quasars.

We investigate the use of the ratio of the Si IV+O IV] to C IV peak fluxes as a method to rehabilitate the C IV-based black hole mass estimates in the spectral energy distribution (SED) atlas of Shang et al. (2011). The quasi-simultaneous optical and UV spectrophotometry available in this data set

is particularly valuable to this investigation, allowing us to consider the H  $\beta$  and C IV spectral regions free of variability concerns. We show that by using both the line width of C IV and peak ratio it is possible to dramatically reduce the scatter between H  $\beta$  and C IV-based black hole mass estimates and derive prescriptions for predicting the H  $\beta$  line width and black hole mass from information in the C IV spectral region.

This investigation is organized as follows. In Section 2 we present the sample and discuss our methods for making spectral measurements. Section 3 presents an analysis of the dependence of velocity line width residuals on the ratio of peak fluxes of Si IV+O IV] to C IV, including a correction for the observed effect that decreases the scatter between C IV and H  $\beta$ -based black hole masses. The results are discussed in the context of other work in Section 4 and conclusions are presented in Section 5. Throughout this work black hole masses and luminosities are calculated using a cosmology with  $H_0 = 70 \text{ km s}^{-1} \text{ Mpc}^{-1}$ ,  $\Omega_\Lambda = 0.7$ , and  $\Omega_m = 0.3$ .

## 2 SAMPLE, DATA, AND MEASUREMENTS

For this work we use the SED sample from Shang et al. (2011). The atlas includes 85 objects, 58 of which are radio-loud (RL) and 27 of which are radio-quiet (RQ), with redshifts in the range  $z = 0.030 - 1.404$  and bolometric luminosities of  $45.1 < \log(L_{bol}) < 47.3$  in units of ergs per second.

Most objects have quasi-simultaneous optical and UV spectrophotometry. All of the objects were observed in the UV either with the *Hubble Space Telescope* Faint Object Spectrograph (FOS) or Space Telescope Imaging Spectrograph (STIS) and most were followed up within a few weeks by low-resolution ground-based optical spectrophotometry from McDonald Observatory or the Kitt Peak National Observatory.

The SED atlas does not comprise a complete sample, but it does include a nearly complete subsample. The PGX subsample has 22 out of 23 Palomar-Green (PG) quasars selected to study the soft X-ray regime (Laor et al. 1994b, 1997), is UV bright, and has  $z \leq 0.4$ . This subsample was presented in Shang et al. (2007), who found that the line widths for these objects do not indicate a purely stratified ionization structure in the BLR. Furthermore, these objects have also been used to illustrate the issues associated with C IV line widths (e.g., Trakhtenbrot & Netzer 2012). The atlas also includes the higher-redshift, higher-luminosity RL subsample and the FUSE subsample that contains mostly radio-quiet objects with redshifts of a few tenths.

This atlas is particularly suited to this investigation for two reasons. First, the quasi-simultaneous optical and UV spectrophotometry makes this sample less susceptible to variability issues than similar investigations (e.g., Trakhtenbrot & Netzer 2012), allowing a meaningful comparison between physical properties calculated from the C IV and H  $\beta$  wavelength regimes. Second, the inclusion of the PGX subsample ensures that the total atlas covers the full range in EV1 properties. This is important because the sample contains a large number of RL sources which are isolated on one end of EV1 with strong [O III] and weak Fe II (e.g., Boroson & Green 1992; Bachev et al. 2004; Sulentic et al.

2007). The sample will exhibit EV1 properties within the range defined by the PGX subsample making our conclusions robust, the fact that the overabundance of RL sources may cause the distribution of those properties to be biased does not compromise this.

The spectra have been corrected for Galactic extinction, reddening, and host contamination in the optical (although these objects are optically bright and the host contribution is minimal). The redshift is determined from the [O III]  $\lambda 5007$  line and the spectra were shifted to the rest frame. Shang et al. (2011) provides more details on these corrections.

Spectral fitting was done by Tang et al. (2012) following the method of Shang et al. (2007). Fitting is done by minimizing  $\chi^2$  between the model and the data using the IRAF package SPECFIT (Kriss 1994). The H  $\beta$ , C IV  $\lambda 1549$ , and Si IV+O IV]  $\lambda 1400$  regions were fit individually with model spectra consisting of a power-law continuum and two Gaussian components per broad emission line. In the case of the Si IV+O IV] blend, which we will hereafter refer to as “ $\lambda 1400$ ”, the fit was made between 1350 and 1460 Å and the power-law continuum is separate from that of C IV. The Gaussians ascribed to Si IV and O IV] were identical except in their centroids which were appropriate for their respective line centers. For the C IV doublet, the Gaussian pairs were also identical except in their centroids and they did not include a component to model emission from the narrow-line region (NLR) because, according to Wills et al. (1993b), there is no strong NLR component present in C IV. The H  $\beta$  broad emission line does include a contribution to emission from the NLR which was modeled with an additional Gaussian that is not included when measuring line widths. A Fe II template derived from the narrow-line Seyfert 1 I Zw1 (Boroson & Green 1992) was also included in the H  $\beta$  region and was allowed to vary in amplitude and velocity width in order to match the observed spectrum.

The spectral fits for  $\lambda 1400$  were done at the same time as the H  $\beta$  and C IV regions but not presented in Tang et al. (2012) so we present them here. A sample spectrum is given in Figure 1 and the results of the fitting are given in Tables 1 and 2.

In most cases, errors on the fit parameters were calculated by Tang et al. (2012) (see also, Shang et al. 2007; Laor et al. 1994a). For spectra with high S/N, the largest uncertainty comes from placing the continuum in each wavelength region rather than formal errors from the fitting process. Therefore, they estimated the errors in the continuum placement by calculating the  $1\sigma$  errors on the flux in the observed spectrum at each end of the local continuum. They then calculate four new continua, corresponding to adding and subtracting the  $1\sigma$  flux errors on each end of the local continuum, and recalculate the measured quantities. The largest positive and negative changes in the measured quantities were taken to be the errors. Uncertainty in the EW and flux in the line measurements for the H  $\beta$  and C IV regions that are not listed here are given in Tang et al. (2012) and calculated via the above method.

The above method for calculating uncertainties is problematic for some parameters (namely line dispersion), which led us to perform a Monte-Carlo fitting procedure similar to that of DiPompeo et al. (2012) to determine the uncertainties on these parameters. The resulting errors on all fit

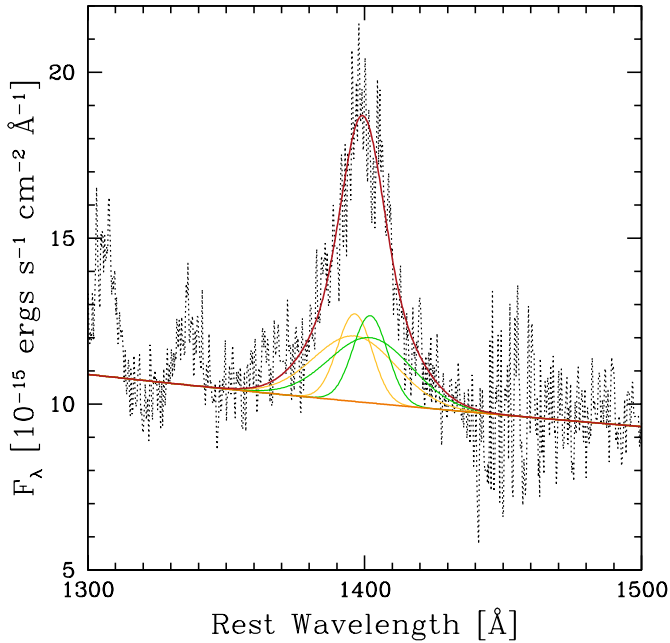


**Figure 1.** Spectral fitting for the wavelength region around  $\lambda 1400$  for PG 1415+451. The observed spectrum is shown by the dotted gray line, the total model spectrum by the red line, the power-law continuum by the orange line, the two Si IV components by the gold lines, and the two O IV components by the green lines.

parameters were very small, indicating that the formal errors on our fitting procedure are small. The uncertainties on each parameter are actually a combination of the fit uncertainties and systematic uncertainties, where the systematic uncertainties likely dominate in our sample.

For the FWHM measurements, which are at the core of this analysis, it is particularly important not to underestimate the measurement uncertainties by ignoring systematic uncertainties. A comparison of measurements of the FWHM of C IV made with similar but not identical methodologies in the literature (Vestergaard & Peterson 2006; Shang et al. 2007) for some objects in our sample shows that measurements typically vary by 15%. This is larger than all but two of the percent errors listed for C IV FWHM (the largest of which is 16%) in Table 2, suggesting that the errors on FWHM may be underestimated. We expect that uncertainty in the line dispersion parameter will be at least as large as for FWHM, indicating that these are likely also at least 15%. While applying our fitting procedure across the literature might yield more consistent results than this, we must also consider the possibility that different fitting procedures behave systematically differently for different line profiles. Thus, in order to be appropriately conservative, we adopt 15% uncertainty for all velocity line width measurements.

Measurements associated with the optical and UV indicators of EV1 are provided in Table 1. Runnoe, Brotherton & Shang (2012) measured continuum luminosities for this sample in the H  $\beta$  and C IV wavelength regimes that are listed in Table 2 along with line width measurements.

### 3 ANALYSIS

#### 3.1 The Eigenvector 1 bias in C IV

The trend of the FWHM of C IV with the ratio  $\text{Peak}(\lambda 1400/\text{C IV})$  illustrated by Wills et al. (1993a) suggests that both EV1 and black hole mass play a role in determining the C IV line profile. Because this effect is not present in H  $\beta$ , we expect that it contributes significantly to the disagreement between velocity widths measured from H  $\beta$  and C IV.

Figure 2 demonstrates that the ratio  $\text{Peak}(\lambda 1400/\text{C IV})$  is correlated with the significant scatter between FWHM of H  $\beta$  and C IV. We distinguish between RL and RQ points in the figure and find that they do not clearly populate separate relationships, though they do tend to occupy opposite ends of EV1.

We performed a regression analysis to describe the dependence of the FWHM residuals on  $\text{Peak}(\lambda 1400/\text{C IV})$  and determined an expression for predicting the H  $\beta$  FWHM. Line fitting in this investigation is done with an ordinary least-squares Y on X (OLS(Y|X)) fit. The OLS(Y|X) method is to be used in instances where X is used to predict Y (Isobe et al. 1990), as is the case for our analysis. In the OLS(Y|X) fit, uncertainties are used only in the Y direction so uncertainties on the peak ratio do not enter into the fit. The assumption that the errors in peak ratio are small certainly seems reasonable given the values in the peak fluxes in Table 1, however if the systematic errors dominate over the errors in the fitting procedure these may be underestimated. Because the velocity width measurements have equal percent uncertainties, the points are all weighted equally in the fit.

In order to determine the uncertainty in the slope and intercept used to predict the FWHM of H  $\beta$ , we employ the model-independent Monte Carlo simulation used in Peterson et al. (1998). This method simulates uncertainties associated with the measurement uncertainties and with the individual points in the sample. For our observed dataset of  $N = 69$  objects we do the following. First, generate  $N$  Y values within the  $1\sigma$  Gaussian uncertainties around the measured values to form a dataset. Then, similar to the “bootstrapping” technique,  $N$  sources are selected randomly from the synthetic dataset, without regard for whether a point has been previously selected. Duplicate points that are sampled multiple times are then discarded from the sample, typically cutting the sample down by the Poisson probability of not selecting any given point, or  $\sim 1/e \approx 37\%$ . After duplicates are discarded, the dataset is fit following the procedure used on the actual data. This process is realized  $10^5$  times to build a distribution in the slope and intercept parameters. The standard deviation of these distributions are taken to be the uncertainties on the slope and intercept.

Equation 1 is the resulting method for estimating the FWHM of the H  $\beta$  line based on UV spectral measurements:

$$\begin{aligned} \log \left[ \frac{\text{FWHM}_{\text{H}\beta, \text{predicted}}}{\text{km s}^{-1}} \right] &= \log \left[ \frac{\text{FWHM}_{\text{C IV}}}{\text{km s}^{-1}} \right] - (0.366 \pm 0.048) \\ &- (0.574 \pm 0.061) \log \left[ \text{Peak} \left( \frac{\lambda 1400}{\text{C IV}} \right) \right]. \end{aligned} \quad (1)$$

This expression treats the RL and RQ sources together. We have investigated the relationships for RL and RQ ob-

Table 1. Eigenvector 1 measurements

Object	$\lambda 1400$ EW Å	$\lambda 1400$ Peak $10^{-15}$ ergs $s^{-1}$ $cm^{-2}$ Å $^{-1}$	$\lambda 1400$ Flux $10^{-15}$ ergs $s^{-1}$ $cm^{-2}$	CIV EW Å	CIV Peak $10^{-15}$ ergs $s^{-1}$ $cm^{-2}$ Å $^{-1}$	CIV Flux $10^{-15}$ ergs $s^{-1}$ $cm^{-2}$	Fe II EW Å	[O III] EW Å
3C 110	12.77 ± 0.26	0.75 ± 0.02	50.87 ± 0.98	107.78	7.84 ± 0.02	363.39	27.08	24.98
3C 175	12.56 ± 0.59	0.43 ± 0.02	37.53 ± 0.95	55.59	3.24 ± 0.02	158.61	21.10	20.05
3C 186	15.70 ± 1.20	0.15 ± 0.02	10.52 ± 0.93	66.50	0.91 ± 0.02	40.18	...	...
3C 207	15.21 ± 0.88	0.38 ± 0.02	12.99 ± 0.94	86.32	2.31 ± 0.02	75.68	60.97	23.34
3C 215	18.88 ± 0.56	0.53 ± 0.02	15.49 ± 0.95	204.60	3.65 ± 0.02	153.49	55.13	47.03
3C 232	14.06 ± 0.24	1.11 ± 0.02	45.03 ± 0.98	33.54	2.30 ± 0.03	100.00	66.87	55.39
3C 254	19.84 ± 1.11	0.33 ± 0.02	13.33 ± 0.93	172.43	2.44 ± 0.02	107.46	102.79	116.51
3C 263	12.52 ± 0.36	2.01 ± 0.02	68.07 ± 0.97	75.51	11.50 ± 0.02	344.69	58.81	20.10
3C 277.1	17.56 ± 0.88	1.07 ± 0.02	30.54 ± 0.94	106.47	6.42 ± 0.02	163.87	103.86	159.40
3C 281	15.83 ± 0.97	0.38 ± 0.02	22.56 ± 0.93	119.67	3.45 ± 0.02	149.15	62.32	46.79
3C 288.1	10.17 ± 0.41	0.13 ± 0.02	7.97 ± 0.96	42.32	0.82 ± 0.02	29.92	121.72	85.38
3C 334	14.67 ± 0.23	0.84 ± 0.02	53.29 ± 0.98	74.98	6.35 ± 0.02	250.62	26.22	40.53
3C 37	34.00 ± 2.54	0.47 ± 0.01	14.54 ± 0.90	252.63	3.64 ± 0.02	97.43	204.08	105.93
3C 446	18.16 ± 6.35	0.10 ± 0.01	6.07 ± 0.87	76.40	0.95 ± 0.02	28.00	...	...
3C 47	18.30 ± 1.14	0.79 ± 0.02	23.17 ± 0.93	172.91	4.98 ± 0.02	212.37	67.08	116.19
4C 01.04	50.12 ± 4.21	0.46 ± 0.01	28.56 ± 0.88	270.36	3.82 ± 0.02	173.77	95.02	39.04
4C 06.69	10.52 ± 0.64	0.70 ± 0.02	38.24 ± 0.95	45.16	3.71 ± 0.02	150.95	42.11	42.89
4C 10.06	21.33 ± 1.31	2.58 ± 0.02	121.57 ± 0.92	114.57	17.44 ± 0.02	598.92	59.90	24.80
4C 11.69	11.98 ± 0.33	0.38 ± 0.02	23.02 ± 0.97	37.41	2.51 ± 0.02	65.65	...	...
4C 12.40	22.88 ± 1.05	0.24 ± 0.02	14.50 ± 0.93	97.16	1.51 ± 0.02	59.50	142.53	40.87
4C 19.44	11.90 ± 0.37	1.52 ± 0.02	44.04 ± 0.96	96.37	11.94 ± 0.02	309.71	69.49	78.62
4C 20.24	25.06 ± 1.03	0.78 ± 0.02	23.20 ± 0.93	185.25	4.76 ± 0.02	136.93	...	...
4C 22.26	16.96 ± 1.26	0.22 ± 0.02	8.78 ± 0.92	180.90	2.00 ± 0.02	78.42	...	...
4C 30.25	17.76 ± 1.24	0.14 ± 0.02	4.56 ± 0.92	146.34	1.09 ± 0.02	32.92	...	...
4C 31.63	8.31 ± 0.43	7.48 ± 0.02	254.54 ± 0.96	39.60	29.13 ± 0.02	1109.30	114.45	6.44
4C 34.47	23.15 ± 1.46	7.47 ± 0.02	201.50 ± 0.92	213.03	67.11 ± 0.02	1802.20	167.16	92.68
4C 39.25	9.75 ± 0.13	0.68 ± 0.02	37.76 ± 1.00	79.99	6.75 ± 0.03	257.07	21.95	15.20
4C 40.24	15.36 ± 1.16	0.22 ± 0.02	5.36 ± 0.93	131.38	1.21 ± 0.02	38.00	...	...
4C 41.21	18.88 ± 0.38	2.46 ± 0.02	99.06 ± 0.96	96.04	14.76 ± 0.02	451.29	61.78	32.98
4C 49.22	24.05 ± 1.25	1.77 ± 0.02	62.16 ± 0.92	178.77	11.80 ± 0.02	379.18	156.32	26.63
4C 55.17	4.32 ± 0.60	0.05 ± 0.02	2.65 ± 0.95	34.57	0.53 ± 0.02	20.00	...	...
4C 58.29	5.59 ± 0.79	0.13 ± 0.02	8.03 ± 1.07	39.43	1.20 ± 0.02	49.09	...	...
4C 64.15	17.89 ± 1.55	0.11 ± 0.02	6.88 ± 0.92	68.54	0.52 ± 0.02	26.00	...	...
4C 73.18	11.58 ± 0.63	6.02 ± 0.02	158.98 ± 0.95	111.79	38.03 ± 0.02	1119.60	41.19	24.41
B2 0742+31	13.29 ± 0.36	1.84 ± 0.02	69.12 ± 0.97	127.78	13.99 ± 0.02	550.29	31.21	41.31
B2 1351+31	7.66 ± 0.83	0.05 ± 0.02	2.89 ± 0.94	47.73	0.39 ± 0.02	14.73	...	...
B2 1555+33	18.84 ± 2.28	0.13 ± 0.01	5.37 ± 0.90	108.54	0.91 ± 0.02	30.00	...	...
B2 1611+34	13.03 ± 1.06	0.24 ± 0.01	10.21 ± 0.74	50.65	1.03 ± 0.01	35.85	0.00	17.44
IRAS F07546+3928	7.83 ± 0.69	6.55 ± 0.02	117.47 ± 0.94	105.34	70.56 ± 0.02	1640.60	188.68	38.01
MC2 0042+101	28.15 ± 4.01	0.17 ± 0.01	7.82 ± 0.90	218.94	1.65 ± 0.02	61.92	0.00	50.37
MC2 1146+111	...	...	...	46.76	0.67 ± 0.02	21.04	111.28	22.07
MRK 506	38.46 ± 1.28	12.91 ± 0.02	454.64 ± 0.92	244.42	75.10 ± 0.02	2670.80	101.49	35.72
MRK 509	24.41 ± 0.09	63.26 ± 0.02	1988.98 ± 1.01	140.75	316.41 ± 0.17	10404.00	99.66	83.64
OS 562	11.70 ± 0.54	0.66 ± 0.02	30.01 ± 0.95	46.38	3.50 ± 0.02	105.04	77.36	14.43
PG 0052+251	15.65 ± 1.00	7.98 ± 0.02	284.58 ± 0.93	137.58	51.26 ± 0.02	2181.00	52.62	53.81
PG 0844+349	15.12 ± 0.21	16.29 ± 0.02	455.52 ± 0.99	48.19	46.03 ± 0.03	1332.70	211.82	7.13
PG 0947+396	11.87 ± 0.72	3.01 ± 0.02	81.63 ± 0.94	95.66	18.56 ± 0.02	590.26	129.44	23.68
PG 0953+414	6.67 ± 0.52	7.74 ± 0.02	178.25 ± 0.95	49.35	42.75 ± 0.02	1150.10	42.99	12.04
PG 1001+054	26.76 ± 0.83	5.23 ± 0.02	104.68 ± 0.94	75.08	10.01 ± 0.02	272.12	202.69	12.11
PG 1100+772	4.32 ± 0.83	3.29 ± 0.02	63.84 ± 0.94	79.68	22.99 ± 0.02	950.62	54.83	42.10
PG 1103-006	14.56 ± 0.85	1.54 ± 0.02	51.79 ± 0.94	55.29	5.18 ± 0.02	181.26	97.99	13.08
PG 1114+445	17.48 ± 1.71	3.04 ± 0.02	110.01 ± 0.91	81.06	15.27 ± 0.02	487.70	48.70	15.75
PG 1115+407	14.19 ± 0.76	6.50 ± 0.02	181.79 ± 0.94	47.59	14.90 ± 0.02	519.46	149.95	8.05
PG 1116+215	15.02 ± 0.47	16.27 ± 0.02	523.42 ± 0.96	71.84	70.19 ± 0.02	2160.80	171.68	16.72
PG 1202+281	39.63 ± 1.95	3.66 ± 0.01	98.11 ± 0.91	306.34	28.91 ± 0.02	711.04	59.75	55.91
PG 1216+069	10.27 ± 0.24	1.99 ± 0.02	68.10 ± 0.98	98.03	17.29 ± 0.02	557.16	41.99	10.49
PG 1226+023	5.91 ± 0.52	55.37 ± 0.02	1447.16 ± 0.95	32.40	222.96 ± 0.03	7417.00	111.46	8.30
PG 1259+593	11.29 ± 0.40	3.21 ± 0.02	112.42 ± 0.96	20.31	4.33 ± 0.02	184.00	403.05	4.45
PG 1309+355	8.25 ± 0.58	3.89 ± 0.02	91.00 ± 0.95	56.31	16.51 ± 0.02	549.79	66.20	17.05
PG 1322+659	7.53 ± 1.46	2.42 ± 0.02	72.00 ± 0.92	54.44	15.67 ± 0.02	454.92	97.48	7.49
PG 1351+640	22.06 ± 0.52	17.53 ± 0.02	358.64 ± 0.95	78.63	49.34 ± 0.02	1296.40	29.26	38.10
PG 1352+183	17.48 ± 1.22	5.13 ± 0.02	174.24 ± 0.92	77.75	20.50 ± 0.02	650.23	112.52	9.68
PG 1402+261	14.05 ± 0.82	9.44 ± 0.02	301.14 ± 0.94	44.60	24.73 ± 0.02	831.74	259.46	2.45
PG 1411+442	17.40 ± 0.40	20.56 ± 0.02	426.44 ± 0.96	44.69	63.08 ± 0.02	911.68	122.90	13.37
PG 1415+451	22.81 ± 2.46	8.63 ± 0.01	229.08 ± 0.90	65.49	23.30 ± 0.02	588.64	210.30	2.68
PG 1425+267	10.30 ± 0.50	1.25 ± 0.02	41.86 ± 0.95	123.53	9.07 ± 0.02	449.43	34.43	31.57
PG 1427+480	16.11 ± 0.64	3.47 ± 0.02	108.83 ± 0.95	77.59	21.38 ± 0.02	463.34	83.29	27.86
PG 1440+356	11.62 ± 0.47	23.43 ± 0.02	489.35 ± 0.96	33.02	78.97 ± 0.02	1246.80	230.09	7.59
PG 1444+407	14.67 ± 0.29	3.91 ± 0.02	132.63 ± 0.97	24.09	6.70 ± 0.02	198.97	287.49	1.49
PG 1512+370	6.95 ± 0.27	0.93 ± 0.02	28.00 ± 0.98	119.28	10.43 ± 0.02	420.14	23.43	58.42
PG 1534+580	16.05 ± 1.74	7.18 ± 0.02	213.60 ± 0.91	142.51	65.41 ± 0.02	1740.30	25.40	114.48
PG 1543+489	18.20 ± 0.22	3.19 ± 0.02	100.46 ± 0.98	39.07	5.69 ± 0.03	209.09	206.92	5.42
PG 1545+210	20.56 ± 0.98	3.58 ± 0.02	143.52 ± 0.93	181.05	26.77 ± 0.02	1047.40	24.95	41.54
PG 1626+554	16.67 ± 1.26	7.21 ± 0.02	281.87 ± 0.92	70.85	30.96 ± 0.02	1012.60	72.18	5.44
PG 1704+608	2.68 ± 0.38	0.42 ± 0.02	23.79 ± 0.96	61.20	11.99 ± 0.02	495.60	13.60	27.68
PG 2214+139	12.94 ± 0.13	15.89 ± 0.02	562.97 ± 0.99	51.88	76.43 ± 0.02	2100.90	173.28	12.43
PG 2251+113	12.12 ± 0.39	3.33 ± 0.02	103.58 ± 0.96	96.91	19.56 ± 0.02	713.28	144.98	28.07
PG 2349-014	10.58 ± 1.82	3.53 ± 0.01	93.80 ± 0.91	155.39	30.32 ± 0.02	1231.60	106.56	32.27
PKS 0112-017	13.00 ± 0.28	0.19 ± 0.02	8.98 ± 0.97	30.81	0.54 ± 0.03	20.00	...	...
PKS 0403-13	15.60 ± 0.62	0.97 ± 0.02	29.98 ± 1.05	138.32	7.92 ± 0.02	213.37	67.08	19.87
PKS 0859-14	10.09 ± 0.62	0.46 ± 0.02	14.73 ± 0.95	48.89	1.80 ± 0.02	59.88	94.14	8.67
PKS 1127-14	12.62 ± 2.13	0.25 ± 0.01	15.00 ± 0.91	25.93	1.03 ± 0.02	30.00	...	...
PKS 1656+053	6.35 ± 0.66	0.40 ± 0.02	17.06 ± 0.95	...	...	...	114.08	3.84
PKS 2216-03	15.36 ± 0.82	0.88 ± 0.02	32.83 ± 0.94	59.31	3.49 ± 0.02	121.23	82.00	31.66
TEX 1156+213	14.69 ± 0.70	1.11 ± 0.02	45.00 ± 0.94	116.09	7.91 ± 0.02	301.97	58.40	17.46

Note – EWs are given in the rest frame and fluxes in the observed frame.

**Table 2.** Physical measurements

Object	$\log \lambda L_{\lambda}(1450\text{\AA})$ ergs s <sup>-1</sup>	$\log \lambda L_{\lambda}(5100\text{\AA})$ ergs s <sup>-1</sup>	$\sigma_{I,CIV}$ km s <sup>-1</sup>	$\sigma_{I,H\beta}$ km s <sup>-1</sup>	$\text{FWHM}_{CIV}$ km s <sup>-1</sup>	$\text{FWHM}_{H\beta}$ km s <sup>-1</sup>	$\text{FWHM}_{\lambda 1400}$ km s <sup>-1</sup>
3C 110	46.43	45.99	5260 ± 789	5431 ± 814	5700 ± 855	12450 ± 1867	13817 ± 2072
3C 175	46.34	46.11	5322 ± 798	9599 ± 1439	6915 ± 1037	20925 ± 3138	17544 ± 2631
3C 186	46.07	45.79	4521 ± 678	...	6290 ± 943	...	14101 ± 2115
3C 207	45.65	45.48	3386 ± 507	5342 ± 801	4935 ± 740	3505 ± 525	4992 ± 748
3C 215	45.02	44.94	5049 ± 757	3475 ± 521	5605 ± 840	6760 ± 1014	4459 ± 668
3C 232	45.87	45.72	4053 ± 608	3328 ± 499	7145 ± 1071	4655 ± 698	6153 ± 923
3C 254	45.63	45.36	5105 ± 765	7142 ± 1071	5205 ± 780	14095 ± 2114	6305 ± 945
3C 263	46.33	46.01	4483 ± 672	4041 ± 606	3310 ± 496	4970 ± 745	5025 ± 753
3C 277.1	45.04	44.67	3333 ± 500	3051 ± 457	3215 ± 482	3835 ± 575	4339 ± 650
3C 281	45.68	45.32	5184 ± 777	4579 ± 686	4865 ± 729	7985 ± 1197	12003 ± 1800
3C 288.1	46.01	45.62	4780 ± 717	3906 ± 585	4015 ± 602	8970 ± 1345	12217 ± 1832
3C 334	46.00	45.58	3983 ± 597	4722 ± 708	5745 ± 861	6345 ± 951	12737 ± 1910
3C 37	45.28	44.89	3225 ± 483	3893 ± 584	3360 ± 504	4280 ± 642	4619 ± 692
3C 446	46.19	46.43	3780 ± 567	...	3390 ± 508	...	12181 ± 1827
3C 47	45.27	44.88	5265 ± 789	6892 ± 1033	5450 ± 817	14005 ± 2100	4415 ± 662
4C 01.04	44.43	44.69	4553 ± 683	4196 ± 629	6665 ± 999	9905 ± 1485	12310 ± 1846
4C 06.69	46.73	46.43	4288 ± 643	2340 ± 351	5620 ± 843	4015 ± 602	10807 ± 1621
4C 10.06	45.85	45.47	4566 ± 684	5922 ± 888	3785 ± 567	4735 ± 710	8366 ± 1254
4C 11.69	46.51	46.38	3527 ± 529	...	3185 ± 477	...	12207 ± 1831
4C 12.40	45.53	45.13	4485 ± 672	2329 ± 349	5300 ± 795	3565 ± 534	12378 ± 1856
4C 19.44	46.30	45.99	3624 ± 543	3152 ± 472	2730 ± 409	4575 ± 686	4367 ± 655
4C 20.24	46.22	45.95	3654 ± 548	...	3525 ± 528	...	4477 ± 671
4C 22.26	45.83	45.52	4390 ± 658	...	5015 ± 752	...	5931 ± 859
4C 30.25	45.64	45.13	3715 ± 557	...	3730 ± 559	...	4806 ± 720
4C 31.63	46.21	45.61	4322 ± 648	2699 ± 404	4840 ± 726	3395 ± 509	5033 ± 754
4C 34.47	45.27	44.97	3785 ± 567	3277 ± 491	2855 ± 428	5015 ± 752	4159 ± 623
4C 39.25	46.25	45.97	4429 ± 664	3538 ± 530	4775 ± 716	6400 ± 960	11040 ± 1656
4C 40.24	45.96	45.74	3265 ± 489	...	4920 ± 738	...	3973 ± 595
4C 41.21	46.27	45.64	3736 ± 560	3170 ± 475	3800 ± 570	3445 ± 516	6075 ± 911
4C 49.22	45.21	44.84	3465 ± 519	2741 ± 411	4535 ± 680	3910 ± 586	5151 ± 772
4C 55.17	45.83	45.72	3777 ± 566	...	6420 ± 963	...	9769 ± 1465
4C 58.29	46.73	46.42	4211 ± 631	...	5745 ± 861	...	12128 ± 1819
4C 64.15	46.14	45.98	5230 ± 784	...	7245 ± 1086	...	12366 ± 1854
4C 73.18	45.80	45.55	3585 ± 537	2704 ± 405	3560 ± 534	3095 ± 464	4172 ± 625
B2 0742+31	45.89	45.77	4475 ± 671	5203 ± 780	4890 ± 733	10690 ± 1603	5623 ± 843
B2 1351+31	46.07	45.81	4728 ± 709	...	3690 ± 553	...	12220 ± 1833
B2 1555+33	45.57	45.39	3785 ± 567	...	4240 ± 636	...	6663 ± 999
B2 1611+34	46.50	46.29	3836 ± 575	3074 ± 461	4625 ± 693	4795 ± 719	6557 ± 983
IRAS F07546+3928	44.76	44.86	3486 ± 522	2999 ± 449	3035 ± 455	2785 ± 417	3624 ± 543
MC2 0042+101	44.99	44.94	4616 ± 692	3517 ± 527	4195 ± 629	8270 ± 1240	7893 ± 1184
MC2 1146+111	45.66	45.52	3926 ± 588	3438 ± 515	3715 ± 557	7835 ± 1175	...
MRK 506	43.88	43.77	3563 ± 534	3248 ± 487	5290 ± 793	4840 ± 726	5408 ± 811
MRK 509	44.51	44.19	3785 ± 567	2645 ± 396	4710 ± 706	3825 ± 573	4886 ± 732
OS 562	46.21	45.82	4234 ± 635	2715 ± 407	3470 ± 520	3305 ± 495	7870 ± 1180
PG 0052+251	45.27	44.88	4589 ± 688	3864 ± 579	5815 ± 872	6460 ± 969	5610 ± 841
PG 0844+349	44.66	44.39	2880 ± 432	2010 ± 301	4550 ± 682	2870 ± 430	4607 ± 691
PG 0947+396	45.15	44.79	3812 ± 571	2822 ± 423	3925 ± 588	4340 ± 651	4977 ± 746
PG 0953+414	45.87	45.38	3239 ± 485	2429 ± 364	3810 ± 571	2990 ± 448	4213 ± 631
PG 1001+054	44.66	44.40	3832 ± 574	1529 ± 229	3130 ± 469	2615 ± 392	3737 ± 560
PG 1100+772	45.90	45.44	4784 ± 717	4158 ± 623	4775 ± 716	9390 ± 1408	3556 ± 533
PG 1103-006	45.67	45.30	4212 ± 631	3187 ± 478	4515 ± 677	5270 ± 790	4964 ± 744
PG 1114+445	44.75	44.80	3942 ± 591	3789 ± 568	3935 ± 590	4825 ± 723	6283 ± 942
PG 1115+407	45.11	44.61	4049 ± 607	1838 ± 275	4585 ± 687	1895 ± 284	5073 ± 761
PG 1116+215	45.69	45.10	3650 ± 547	2167 ± 325	3865 ± 579	2975 ± 446	5682 ± 852
PG 1202+281	44.48	44.50	3932 ± 589	5100 ± 765	2945 ± 441	4950 ± 742	4882 ± 732
PG 1216+069	45.62	45.48	5141 ± 771	3376 ± 506	3105 ± 465	5950 ± 892	6216 ± 932
PG 1226+023	46.45	45.97	3724 ± 558	2791 ± 418	4530 ± 679	3405 ± 510	4571 ± 685
PG 1259+593	46.26	45.69	4105 ± 615	3664 ± 549	6880 ± 1032	4035 ± 605	5311 ± 796
PG 1309+355	45.21	45.07	4775 ± 716	4632 ± 694	2815 ± 422	3640 ± 546	4246 ± 636
PG 1322+659	45.07	44.70	3510 ± 526	1776 ± 266	3690 ± 553	3285 ± 492	4544 ± 681
PG 1351+640	44.71	44.90	2953 ± 442	3355 ± 503	4050 ± 607	6205 ± 930	3790 ± 568
PG 1352+183	44.96	44.52	3827 ± 574	3162 ± 474	3755 ± 563	4210 ± 631	5981 ± 897
PG 1402+261	45.41	44.84	3894 ± 584	1992 ± 298	4550 ± 682	2100 ± 315	6397 ± 959
PG 1411+442	44.86	44.67	2003 ± 300	3465 ± 519	2040 ± 306	2800 ± 420	3921 ± 588
PG 1415+451	44.70	44.45	2656 ± 398	1950 ± 292	3725 ± 558	2560 ± 384	4711 ± 706
PG 1425+267	45.54	45.28	5076 ± 761	6235 ± 935	7060 ± 1059	9875 ± 1481	6565 ± 984
PG 1427+480	45.21	44.74	2758 ± 413	3975 ± 596	2835 ± 425	2405 ± 360	5796 ± 869
PG 1440+356	44.97	44.60	1959 ± 293	1109 ± 166	2130 ± 319	1745 ± 261	3917 ± 587
PG 1444+407	45.55	45.17	3428 ± 514	2037 ± 305	4425 ± 663	2750 ± 412	6224 ± 933
PG 1512+370	45.55	45.15	5238 ± 785	5458 ± 818	3970 ± 595	7690 ± 1153	5628 ± 844
PG 1534+580	43.61	43.37	3239 ± 485	2888 ± 433	3790 ± 568	4505 ± 675	4609 ± 691
PG 1543+489	45.80	45.38	3842 ± 576	1491 ± 223	5625 ± 843	2320 ± 348	5424 ± 813
PG 1545+210	45.39	45.07	4654 ± 698	3382 ± 507	4560 ± 684	6885 ± 1032	6148 ± 922
PG 1626+554	45.06	44.61	4291 ± 643	2998 ± 449	3815 ± 572	4390 ± 658	6502 ± 975
PG 1704+608	45.91	45.72	5340 ± 801	4637 ± 695	4015 ± 602	10465 ± 1569	11557 ± 1733
PG 2214+139	44.84	44.54	3678 ± 551	3137 ± 470	2690 ± 403	5845 ± 876	6551 ± 982
PG 2251+113	45.73	45.53	4234 ± 635	2996 ± 449	4805 ± 720	4060 ± 609	4660 ± 699
PG 2349-014	45.09	44.78	4211 ± 631	3728 ± 559	5675 ± 851	6325 ± 948	4476 ± 671
PKS 0112-017	46.44	46.07	4019 ± 602	...	5030 ± 754	...	8572 ± 1285
PKS 0403-13	45.69	45.53	3977 ± 596	2856 ± 428	3325 ± 498	3735 ± 560	4577 ± 686
PKS 0859-14	46.68	46.45	3737 ± 560	5260 ± 789	4520 ± 678	4615 ± 692	4737 ± 710
PKS 1127-14	46.50	46.21	3501 ± 525	...	3695 ± 554	...	12263 ± 1839
PKS 1656+053	46.44	46.26	...	2832 ± 424	...	3510 ± 526	6933 ± 1040
PKS 2216-03	46.38	46.31	4504 ± 675	2962 ± 444	3600 ± 540	4415 ± 662	5580 ± 837
TEX 1156+213	45.36	45.00	5129 ± 769	3604 ± 540	3880 ± 582	7740 ± 1161	6156 ± 923

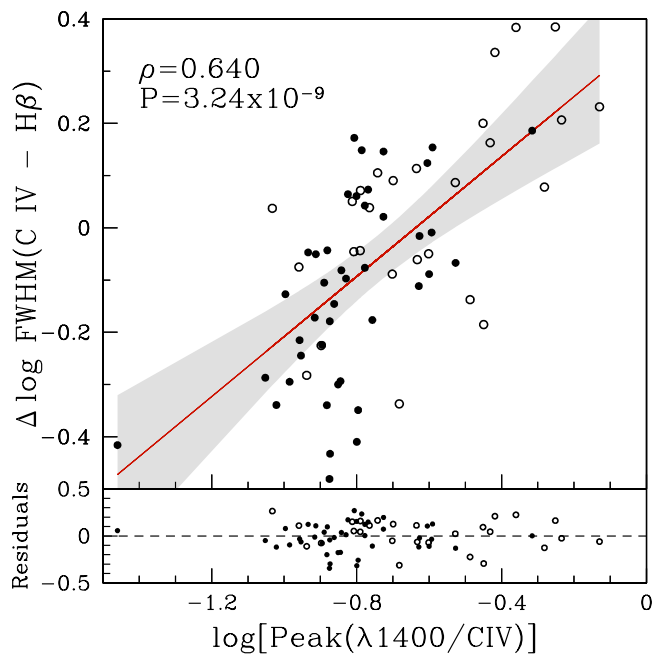


**Figure 2.** Residuals in FWHM for C IV and H  $\beta$  versus Peak( $\lambda 1400/C IV$ ) (top) and residuals in the fit (bottom). The Spearman Rank correlation coefficient and associated probability that this distribution of points occurs by chance are listed in the upper left corner. The significant correlation indicates that the disagreement between C IV and H  $\beta$  line widths that we hope to reduce depends on Peak( $\lambda 1400/C IV$ ). The fitted line is given in red with the shaded region indicating the 95% confidence interval. Radio-loud objects are indicated by solid circles and open circles are radio-quiet.

jects separately and find that they are not significantly different within the 95% confidence intervals, as is suggested by the distribution of RL and RQ points in Figure 2. We note that, in the case of the RL sources, the correlation appears to be driven by two outliers in the peak ratio. A Monte Carlo bootstrapping simulation that would likely reveal any sample dependence of RL correlation is beyond the scope of this paper, but we do wish to draw the readers attention to this possible caveat.

The FWHM predicted for H  $\beta$  based on C IV and  $\lambda 1400$  shows less scatter with the true FWHM of H  $\beta$  than does C IV alone. Figure 3 shows the relationship between H  $\beta$  and C IV FWHM compared to H  $\beta$  and the predicted H  $\beta$  from Equation 1. Independent of the assumed relationship between FWHM of C IV and H  $\beta$ , the initial scatter between them is 0.20 dex. This is reduced to 0.15 dex and the points become fairly well centered around the one-to-one relationship by using Equation 1. This scatter reduction is in the dispersion of the distribution of the  $\log(\text{FWHM})$  residuals only, and is independent of the assuming a relationship between C IV and H  $\beta$  FWHM. Our goal here is to be able to effectively predict the H  $\beta$  FWHM, thus the reduction in scatter allows a more precise measurement.

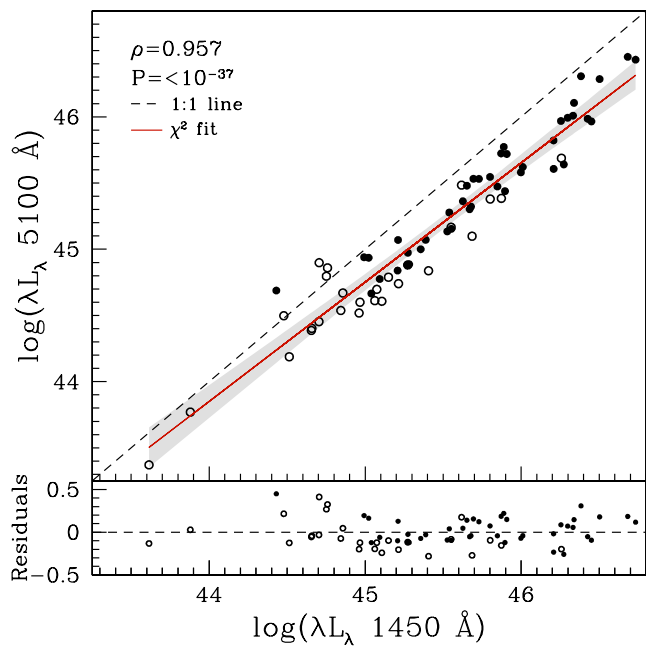


**Figure 4.** 5100  $\text{\AA}$  luminosity versus 1450  $\text{\AA}$  luminosity (top) and residuals in the fit (bottom). The dashed black line indicates where the luminosities are the same and the solid red line is the fitted line with the shaded region indicating the 95% confidence interval. Spearman Rank correlation coefficient and associated probability of finding this distribution of points by chance are listed in the upper left corner. Radio-loud objects are indicated by solid circles and open circles are radio-quiet.

### 3.2 Improved black hole masses

In order to propagate the predicted H  $\beta$  FWHM into a black hole mass estimate, we derived a relationship for predicting the 5100  $\text{\AA}$  luminosity from the 1450  $\text{\AA}$  luminosity. Figure 4 shows that  $\lambda L_{\lambda}(5100 \text{\AA})$  and  $\lambda L_{\lambda}(1450 \text{\AA})$  are very significantly correlated, indicating that the 1450  $\text{\AA}$  luminosity is a good proxy for the 5100  $\text{\AA}$  luminosity. When fitting the luminosities, we weighted each point equally. The fitted line, determined using the same OLS( $Y|X$ ) fitting procedure, shown in Figure 4 is:

$$\log \left[ \frac{\lambda L_{\lambda}(5100 \text{\AA})_{\text{predicted}}}{\text{ergs s}^{-1}} \right] = (0.901 \pm 0.028) \log \left[ \frac{\lambda L_{\lambda}(1450 \text{\AA})}{\text{ergs s}^{-1}} \right] + (4.198 \pm 1.265). \quad (2)$$

The uncertainties on the slope and intercept are calculated via the same Monte Carlo method, assuming 5% error in the luminosities consistent with Shang et al. (2007).

With the ability to predict the 5100  $\text{\AA}$  luminosity and H  $\beta$  line width from UV spectral parameters, comes the possibility of better predicting the black hole mass using spectral properties in the C IV wavelength region. We calculated rehabilitated C IV masses from the predicted FWHM of H  $\beta$  using Equation 1, the predicted 5100  $\text{\AA}$  continuum luminosity using Equation 2, and the H  $\beta$  scaling relationship from Vestergaard & Peterson (2006). We found better agreement between H  $\beta$ -based black hole masses and those calculated

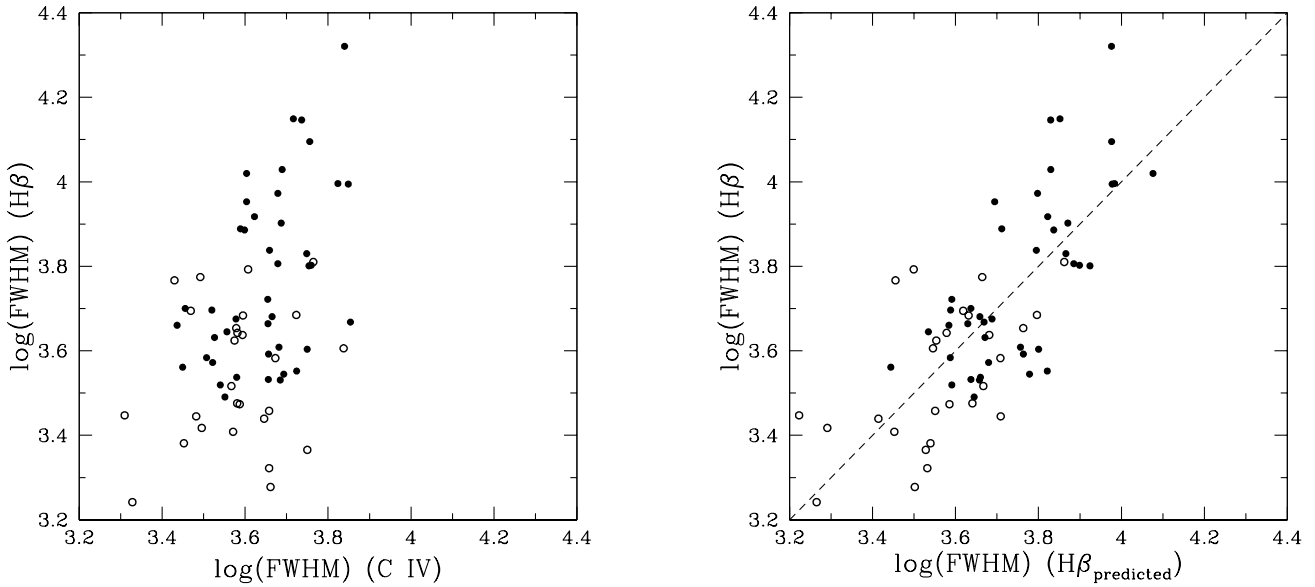


**Figure 3.** The FWHM of  $H\beta$  versus C IV (left panel) and versus the FWHM predicted for  $H\beta$  based on UV spectral information (right panel). In the left panel, we do not expect the line widths to be equal and rather illustrate the scatter between  $H\beta$  and C IV measurements. In the right panel, we have used Equation 1 to predict the  $H\beta$  line width and expect the data to fall around the dashed one-to-one line. The scatter decreases from 0.20 to 0.15 dex after including a  $\text{Peak}(\lambda 1400/\text{C IV})$  term and the points are fairly evenly distributed around the one-to-one line. Radio-loud objects are indicated by solid circles and open circles are radio-quiet.

from C IV and  $\text{Peak}(\lambda 1400/\text{C IV})$  than those calculated from C IV alone. Figure 5 shows the before and after with  $H\beta$  versus C IV and  $H\beta$  versus predicted  $H\beta$ -based black hole masses. The improvement is significant, with a reduction in scatter from 0.43 dex to 0.33 dex. This method is independent of the choice in scaling relationship; it is not necessary to use the Vestergaard & Peterson (2006) scaling relationship, any relation using FWHM  $H\beta$  and 5100 Å continuum luminosity could be substituted.

The reduction in scatter between  $H\beta$  and C IV-based black hole masses can also be seen in the reduction in the width of the distribution of mass residuals. Figure 6 shows “before” and “after” histograms for the FWHM-based black hole mass estimates. It is clear that the scatter is reduced by the width reduction in the distribution.

Black hole masses have already been calculated for thousands of objects using the C IV prescription from Vestergaard & Peterson (2006), for example in the catalog of Shen et al. (2011). In these cases, it is more straightforward to correct the pre-calculated black hole mass than to propagate through the predicted optical measurements. We performed a regression analysis on the black hole mass residuals versus  $\text{Peak}(\lambda 1400/\text{C IV})$  (Figure 7). We followed an identical fitting procedure here as for the FWHM residuals, with all of the uncertainty propagated from the velocity line widths and thus all points weighted equally in the fit. Equation 3 gives the correction to pre-calculated black hole masses already derived from C IV measurements:

$$\log \left[ \frac{M_{BH}(H\beta_{\text{predicted}})}{M_{\odot}} \right] = \log \left[ \frac{M_{BH}(\text{C IV})}{M_{\odot}} \right] - (0.734 \pm 0.112) - (1.227 \pm 0.136) \log \left[ \text{Peak} \left( \frac{\lambda 1400}{\text{C IV}} \right) \right] \quad (3)$$

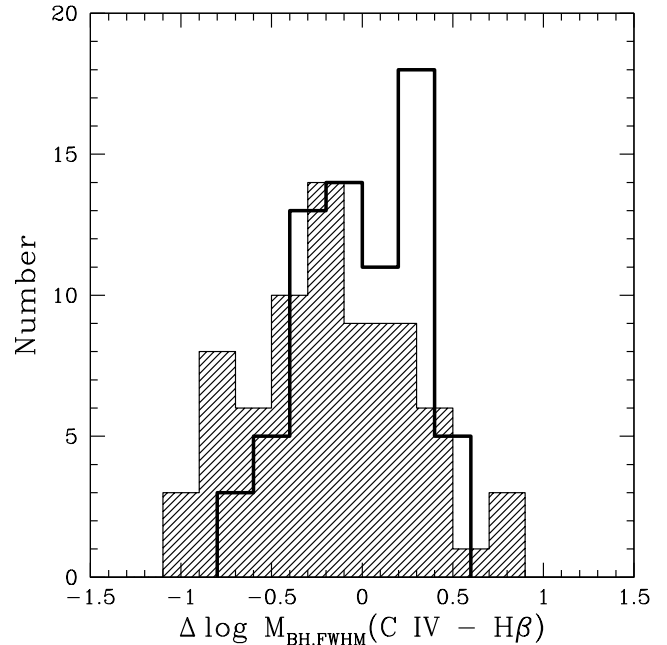


**Figure 6.** Before and after histograms of the residuals between black hole masses derived from FWHM. The shaded histogram shows black hole mass residuals “before”, using the difference between C IV and  $H\beta$ -based masses. The thick histogram shows black hole mass residuals “after”, using the difference between predicted  $H\beta$  (using Equations 1 and 2) and  $H\beta$ -based masses. The primary effect of predicting the FWHM of  $H\beta$  and using it to calculate black hole mass is a reduction in width of the distribution.



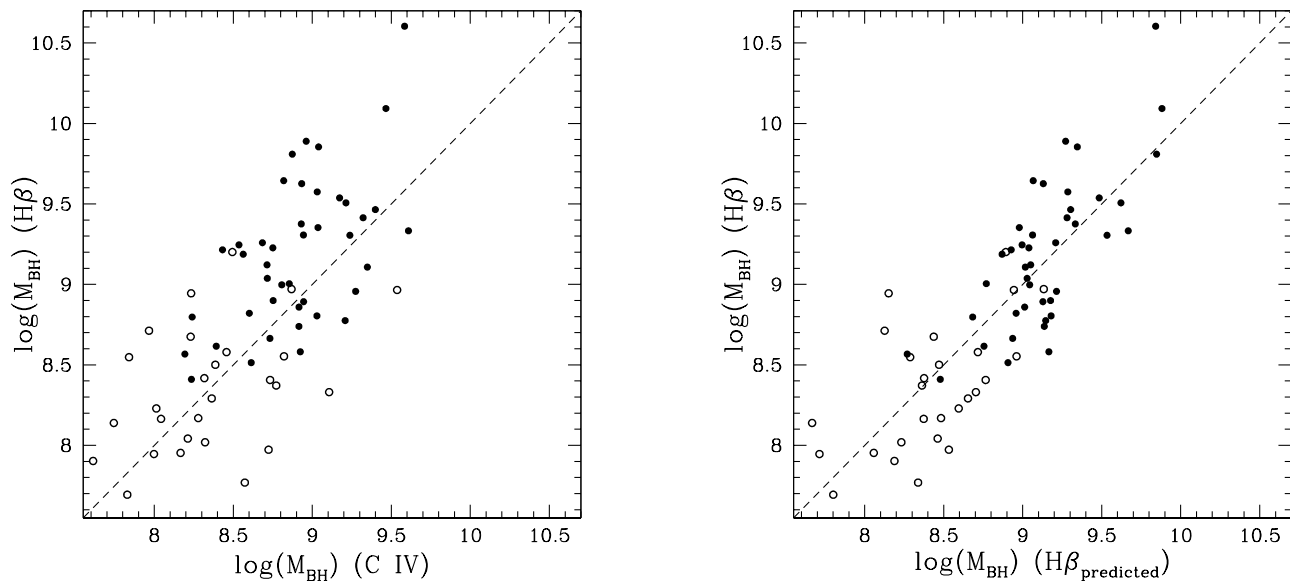


**Figure 5.**  $H\beta$ -based black hole masses versus C IV-based black hole masses (left panel) and the mass calculated from the predicted  $H\beta$  based on UV spectral information (right panel). The one-to-one line is shown. The scatter, originally 0.43 dex in the left panel, is reduced to 0.33 dex by including Peak( $\lambda 1400/C\text{ IV}$ ) and Equations 1 and 2 when calculating black hole mass from spectral information in the C IV region. Radio-loud objects are indicated by solid circles and open circles are radio-quiet.

This expression assumes the C IV single-epoch scaling relationship of Vestergaard & Peterson (2006) and the resulting predicted  $H\beta$  black hole masses is akin to using the  $H\beta$  scaling relationship from the same authors. The reduction in scatter achieved by using this correction is comparable to propagating the predicted optical measurements through the mass scaling relationship, although this method is less flexible because you cannot choose your mass scaling relationship.

A new mass scaling relationship for C IV based on an updated reverberation mapping sample and methodology has recently become available from Park et al. (2013). We do not re-derive Equation 3 for the new scaling relationship since the motivation for a ready-made mass correction was backwards compatibility with catalogs like Shen et al. (2011). The effect of adopting this new mass scaling relationship in our sample is to increase the initial scatter between  $H\beta$  and C IV-based masses from 0.43 to 0.45 dex. Points in the left panel of Figure 5 move to the left, generally farther from the one-to-one line and the scatter is increased. Thus, the reduction in scatter achieved by correcting Park et al. (2013) C IV-based masses with Equations 1 and 2 is even more significant than for masses calculated from Vestergaard & Peterson (2006).

### 3.3 An alternative measure of line width

Line dispersion is often used for calculating black hole masses instead of FWHM (Peterson et al. 2004). Because of the contaminating emission in the C IV line, line dispersion is often preferred for estimating black hole masses in high-redshift objects. With detailed simulations, Denney et al. (2009) show that line dispersion measurements are much less susceptible to contamination from low-velocity, non-virialized gas. When a contaminating low-velocity compo-

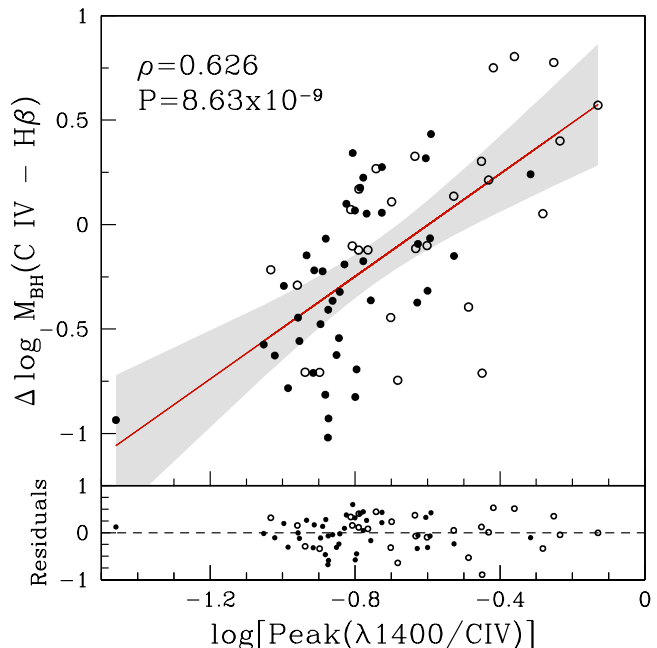


**Figure 7.** Residuals in  $M_{BH}$  for C IV and  $H\beta$  versus the Peak( $\lambda 1400/C\text{ IV}$ ) (top) and residuals in the fit (bottom). The Spearman Rank correlation coefficient and associated probability that this distribution of points occurs by chance are listed in the upper left corner. The significant correlation indicates that there is a Peak( $\lambda 1400/C\text{ IV}$ ) dependence in the mass residuals similar to what was found for the FWHM. The fitted line is given in red with the shaded region indicating the 95% confidence interval. Radio-loud objects are indicated by solid circles and open circles are radio-quiet.

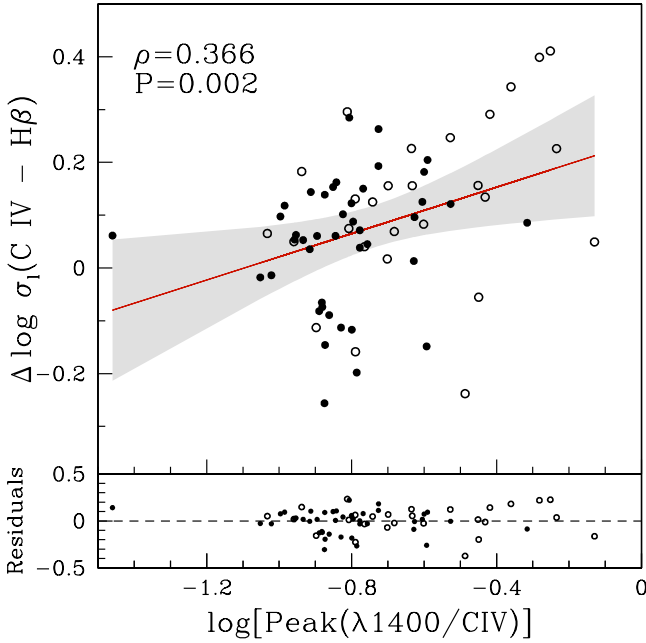


**Figure 8.** Residuals in line dispersion for C IV and H  $\beta$  versus Peak( $\lambda 1400/\text{C IV}$ ). The Spearman Rank correlation coefficient and associated probability that this distribution of points occurs by chance are listed in the upper left corner. The correlation is significant at about the  $3\sigma$  level, much less than for FWHM. Radio-loud objects are indicated by solid circles and open circles are radio-quiet.

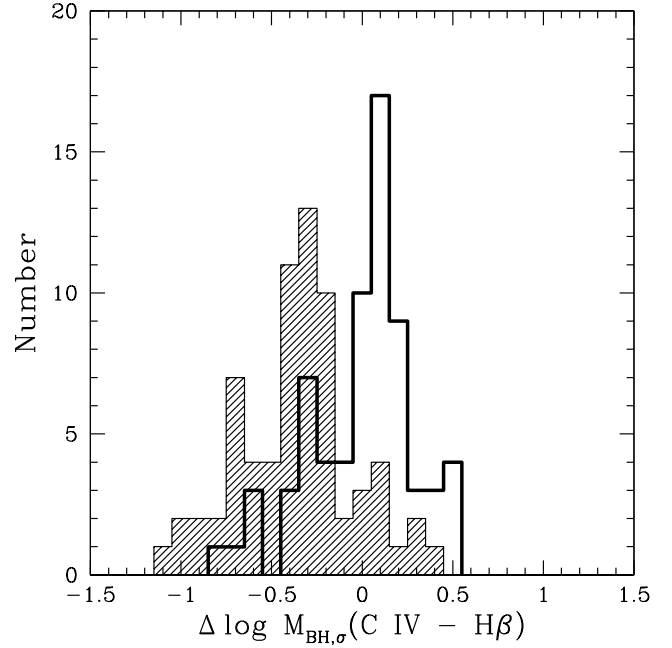
ment is strong in the C IV line, the peak of the emission line shoots up although the base of the line remains largely unchanged. A measurement of FWHM in such a line will give a value that is artificially narrow as the “half maximum” is much higher than it would otherwise would have been. In these cases, the width of the contaminating component is being probed instead of the virialized base that is desired for black hole mass estimates.

Given this, it is not surprising that the residuals in line dispersion between the C IV and H  $\beta$  emission lines are much less significantly correlated with Peak( $\lambda 1400/\text{C IV}$ ) than for FWHM, although the correlation is still significant as seen in Figure 8.

The scatter in the relationship between line dispersion residuals and Peak( $\lambda 1400/\text{C IV}$ ) make a correction less effective than for FWHM. Equation 4 gives the predicted line dispersion for H  $\beta$  based on the C IV line dispersion and Peak( $\lambda 1400/\text{C IV}$ ) that was derived via the same OLS(Y|X) fitting procedure and Monte Carlo error simulation that are used throughout this work:

$$\log \left[ \frac{\sigma_{l, \text{C IV, predicted}}}{\text{km s}^{-1}} \right] = \log \left[ \frac{\sigma_{l, \text{C IV}}}{\text{km s}^{-1}} \right] - (0.241 \pm 0.055) \\ - (0.220 \pm 0.068) \log \left[ \text{Peak} \left( \frac{\lambda 1400}{\text{C IV}} \right) \right]_4$$

The reduction in scatter between H  $\beta$  and C IV-based black hole masses estimated using line dispersion is minimal, on the order of 0.02 dex.



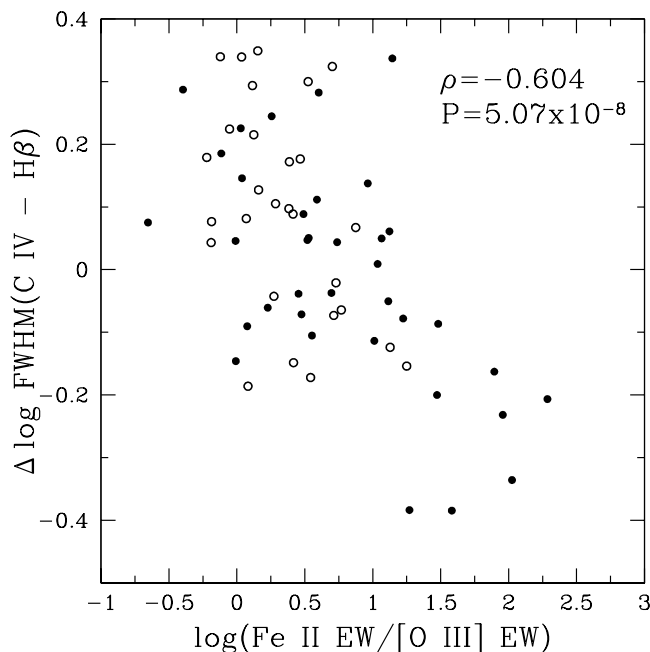
**Figure 9.** Before and after histograms of the residuals between masses derived from line dispersion. The shaded histogram shows black hole mass residuals “before”, using the difference between C IV and H  $\beta$ -based masses. The thick histogram shows black hole mass residuals “after”, using the difference between predicted H  $\beta$  (using Equations 2 and 4) and H  $\beta$ -based masses. Predicting H  $\beta$  line dispersion shifts the distribution to zero, but does not decrease the width appreciably.

Figure 9 shows the distribution in mass residuals calculated from line dispersion for C IV–H  $\beta$  and predicted H  $\beta$ –H  $\beta$ . The distribution is initially relatively narrow, but offset from zero. The result of predicting the H  $\beta$  mass from C IV line dispersion is largely to remove that offset, the width of the distribution is not appreciably reduced. We have attributed this offset to the Peak( $\lambda 1400/\text{C IV}$ ) effect, but we note that there are other possibilities that we discuss further in Section 4.

### 3.4 Eigenvector 1 Indicators

The correction we have derived is thus far is purely empirical, but the inclusion of Peak( $\lambda 1400/\text{C IV}$ ) among the properties correlated in EV1 suggests an origin for the effect. Eigenvector 1 was defined by Boroson & Green (1992) based on measurements of optical spectral properties; variation in EV1 is often described by a continuum in the ratio EW(Fe II/[O III]). Thus, in order to evaluate the source of the dependence of H  $\beta$  and C IV line width residuals on Peak( $\lambda 1400/\text{C IV}$ ), we investigate whether the effect holds for EW(Fe II/[O III]).

Figure 10 shows that the FWHM residuals depend strongly on EW(Fe II/[O III]), with a correlation that is comparable in significance to the one found for Peak( $\lambda 1400/\text{C IV}$ ). This indicates that it is indeed EV1 in addition to black hole mass that contributes to determining the velocity width of the C IV line profile.



**Figure 10.** Residuals in FWHM for C IV and H $\beta$  versus EW(Fe II/[O III]). The Spearman Rank correlation coefficient and associated probability that this distribution of points occurs by chance are listed in the upper left corner. The correlation is comparable in significance to that found for Peak( $\lambda$ 1400/C IV), indicating that the correction derived here is an EV1 effect. Radio-loud objects are indicated by solid circles and open circles are radio-quiet.

EV1 is a suite of spectral properties, so in addition to Peak( $\lambda$ 1400/C IV) and the shape of C IV there are many UV measurements that are strongly correlated with optical EV1 (e.g., Brotherton & Francis 1999). It is not necessary to restrict our analysis to Peak( $\lambda$ 1400/C IV) if another spectral property yields a better mass correction. Because of the practical applications of this work, we were particularly interested in EV1 indicators that are simple to measure and can be obtained with limited wavelength coverage. This rules out UV EV1 indicators like the blueshift of C IV; without sufficient wavelength coverage obtaining a reliable rest frame for the object and thus establishing the blueshift may be difficult. We investigated three UV spectral ratios to compare their ability to predict the optical EV1 indicator: the ratios of peak flux, EW, and flux in the line for  $\lambda$ 1400/C IV. We found that, of these, Peak( $\lambda$ 1400/C IV) is most significantly correlated with EW(Fe II/[O III]) (Figure 11) as well as the FWHM residuals.

## 4 DISCUSSION

### 4.1 Data quality and sample selection

The rehabilitation of black hole mass estimates derived from the FWHM of C IV has significant implications for calculating black hole masses in large numbers of objects. Denney et al. (2013) shows that, until now, the most reliable C IV-based black hole mass estimates required a measure-

ment of line dispersion. The line dispersion measurement is less sensitive to the presence of a core component in the C IV line, and with a shape correction the contamination can be accounted for to some degree. However, line dispersion measurements are incredibly sensitive to the information in the wings of the emission line which can be lost in low S/N data. The low signal to noise of survey-quality data introduces issues for line dispersion measurements, namely that an accurate measurement cannot be obtained. Using FWHM-based black hole masses and applying the shape correction requires a measure of line dispersion, and thus high-quality data.

The introduction of a peak ratio UV EV1 correction to a C IV FWHM mass provides a robust way of measuring more accurate masses from the UV spectral region. FWHM measurements do not suffer as much from these S/N constraints, making them ideal for estimating black hole mass in survey-quality data. A correction to estimate the strength of the core component in the C IV line based on a peak ratio is easy to measure and more robust to low signal to noise, enabling reliable black hole mass estimates for thousands of high-redshift objects in surveys like the Sloan Digital Sky Survey (SDSS).

Denney et al. (2009) performed extensive simulations on the effects of characterizing line widths in data with a variety of S/N ratios. They found that, in low S/N spectra, the ability to characterize the line width is compromised. Furthermore, depending on the procedure used to make the measurement, this can result in either over or underestimated line widths, although for FWHM an underestimate is most common. This discrepancy has the potential to create an offset between C IV and H $\beta$ -based black hole masses that is buried in the black hole mass scaling relations. If this effect is present, it has been wrapped into the correction for the EV1 bias. This should be noted, but is not necessarily the most likely outcome or an issue if it has occurred. According to Denney et al. (2009), the effect of allowing a contaminating narrow, non-virial component in the emission line is larger than S/N effects and Denney (2012) has verified the presence of a shape bias in black hole estimates based on C IV. Finally, for any investigation using spectra similar to ours, the initial offset in the mass residuals from zero exists when applying the Vestergaard & Peterson (2006) scaling relations and the improvement still stands whether we attribute it to measurement issues or EV1. Brotherton et al. (in prep) will perform a more quantitative determination of the amount of improvement that is due exclusively to EV1.

We also note that any C IV-based black hole mass scaling relationship created from a sample that does not have a representative EV1 average will result in biased black hole masses. This is equivalent to the “shape bias” suggested by Denney (2012). Figure 5 (left) shows that the distribution of points in the plot of H $\beta$  versus C IV derived masses using the relationships of Vestergaard & Peterson (2006) are not evenly spread around the one-to-one line as expected. While some of this effect may result from the combination of measurement and S/N bias (e.g., Denney et al. 2009), we also expect a bias since the reverberation sample does not have a representative distribution in EV1, and in particular are deficient in objects at the strong Fe II/weak [O III] end. We will quantitatively investigate this effect in an upcoming paper (Brotherton et al. in prep.).

In light of S/N concerns for C IV, we consider whether

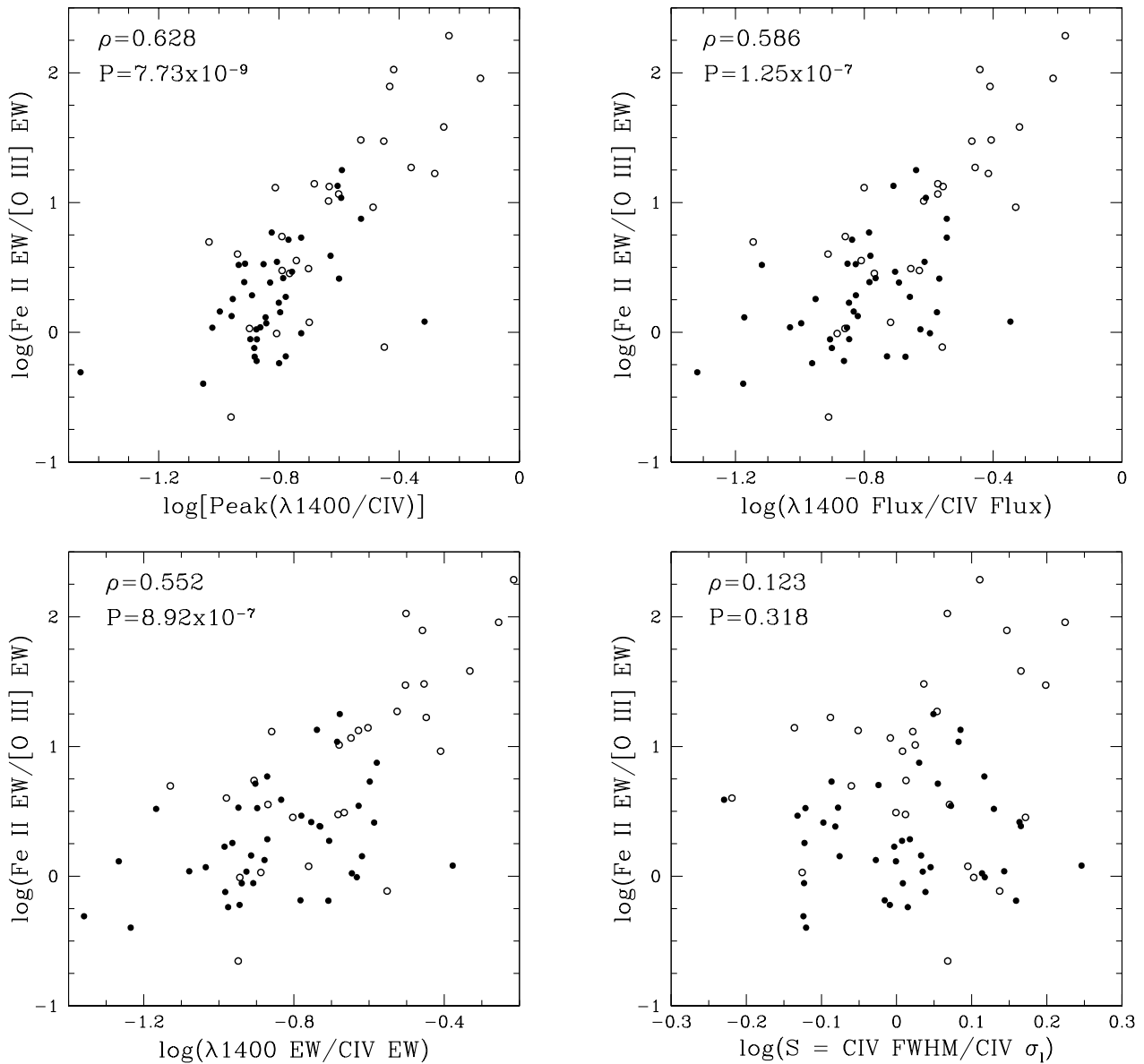


**Figure 11.** The optical EV1 indicator against four UV EV1 indicators. The Spearman Rank correlation coefficient ( $\rho$ ) and associated probability ( $P$ ) that the points will be thus distributed by chance is listed in the upper left corner. The ratio of the  $\lambda 1400$  to CIV peaks (top left panel) is the best proxy for the optical EV1 indicator. Radio-loud objects are indicated by solid circles and open circles are radio-quiet.

the success of our black hole correction might depend on the S/N of the spectrum to which it is applied. Figure 12 is identical to Figure 5 except that the sources have been color coded into three S/N bins ( $6 < S/N < 21$ ,  $21 < S/N < 30$ , and  $30 < S/N < 72$ ), each with an equal number of objects. In general, it does not appear that the sources in any S/N bin are isolated in mass or distance from the one-to-one relationship. There does seem to be an absence of higher-S/N sources with too-small CIV black hole masses (upper right of the left panel), but this is the opposite of what is expected to result from an S/N bias. According to Denney et al. (2009), FWHM tends to be underestimated in low-S/N data, thus we might expect an abundance of low-S/N objects in this region of the plot. There is no trend in the

scatter between the  $H\beta$  masses and the predicted  $H\beta$  masses in the S/N bins: the final scatter is 0.31, 0.38, and 0.31 dex for the high, medium, and low-S/N bins, respectively. Given that all of our data are fairly high S/N, above the  $S/N \sim 5$  cutoff suggested by Denney et al. (2009) for FWHM calculations, this result is not surprising.

## 4.2 The broad line region

The FWHM of  $H\beta$ , which is reliable for probing virialized gas and estimating black hole masses, depends on orientation as indicated by the radio core dominance (Wills & Browne 1986). The FWHM of CIV shows no such dependence, although Vestergaard (2002) shows that the full

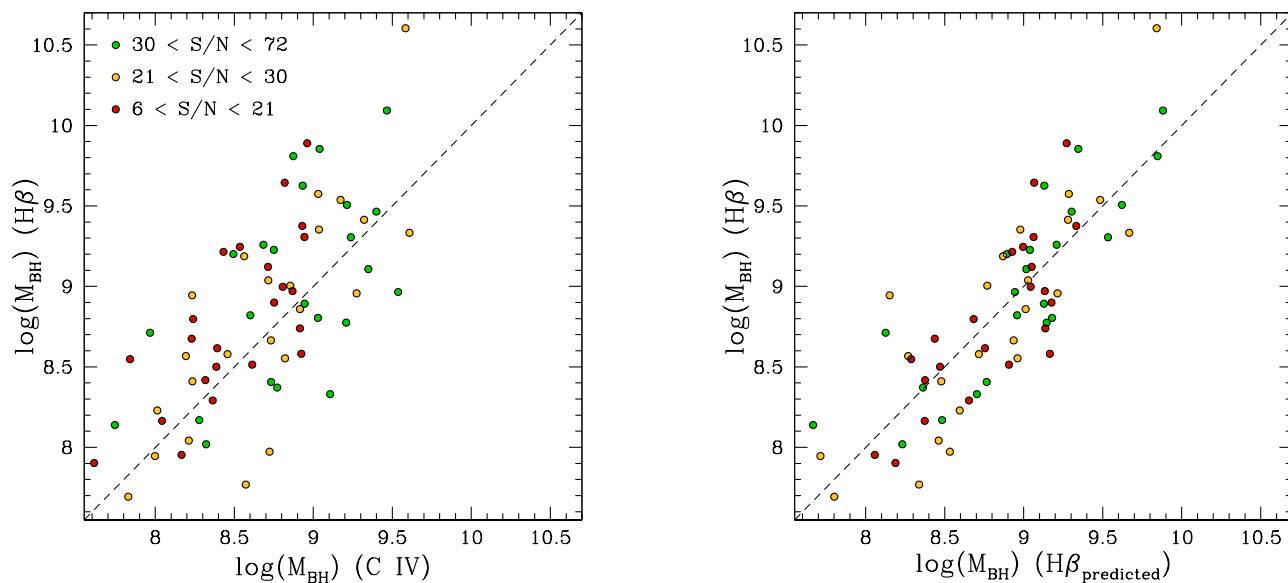


**Figure 12.**  $H\beta$ -based black hole masses versus C IV-based black hole masses (left panel) and the mass calculated from the predicted  $H\beta$  based on UV spectral information (right panel) color coded by S/N. The one-to-one line is shown. Red points indicate objects with the lowest S/N, yellow points have intermediate S/N, and green points have the highest S/N.

width at one quarter maximum (FWQM) does depend on orientation. This behavior in the C IV line is likely the result of the two different components of the line having different orientation dependencies. The virialized component is orientation dependent, as with  $H\beta$ , and is targeted by FWQM which probes the base of the line where this component dominates emission. The non-virial component is independent of orientation and is targeted by FWHM which probes higher in the line where the line width is sensitive to the emission from non-virial gas. In this scenario, once the FWHM of C IV has been corrected for a non-virial contribution to emission, it should depend on orientation. An investigation of this prediction is currently underway (Runnoe et al. in prep.)

One model that is often invoked to explain the two-component structure of the C IV emission was proposed by Wills et al. (1993a) and has the BLR is split into two structures, the very broad line region (VBLR) and the intermediate line region (ILR). Brotherton et al. (1994) compared VBLR and ILR spectra with the results of photoionization models and found that the VBLR is located nearer to the continuum source and is denser than the ILR. They predict that C IV should have a strong ILR contributions whereas  $H\beta$  and the  $1400 \text{ \AA}$  feature will not. The ILR emission is not consistent with emission from the traditional NLR as the physical parameters required to create the observed emission are different, with the ILR having higher densities (Brotherton et al. 1994) and larger velocity widths (Brotherton et al. 1994; Denney 2012). In this model scenario, the non-reverberating, low-velocity core component in the C IV line is attributed to the ILR and creates the peaky C IV line profiles. Wills et al. (1993a) posits that this emission may also originate in a biconical outflow, which is not mutually exclusive to a contribution from ILR emission. This type of multi-component velocity model shows good agreement with observed C IV profiles. Bachev et al.

(2004) observes a distinct VBLR component in objects with low-redshift, composite spectra with small  $\text{EW}(\text{Fe II}/[\text{O III}])$ , although they attribute the low-velocity emission to a traditional NLR region in their decomposition of the line. The ILR is found to agree with with observed C IV line profiles in the literature (e.g., Wills et al. 1993a; Brotherton et al. 1994; Denney 2012).

The goal of this work is to progress in our ability to measure physical properties of quasars with the highest accuracy and precision possible. Other investigations have already taken steps in this direction, including Runnoe, Brotherton & Shang (2012) and Assef et al. (2011) who provide prescriptions for removing an orientation and color bias, respectively, from black hole mass calculations. These investigations suggest that future progress can be made by determining sources of scatter between black hole mass estimates and including those sources in our measurements of physical parameters.

## 5 CONCLUSIONS

Black hole masses estimated from the C IV emission line have large scatter compared to  $H\beta$ -based masses caused by a non-virialized component, consistent with a contribution from the ILR in the C IV line that is weak or absent from  $H\beta$ . The strength of the non-virial component of the C IV line is known to scale with indicators of EV1, allowing it to be separated from the virial C IV emission. Using the quasi-simultaneous optical and UV spectra from the SED atlas of Shang et al. (2011), we investigated methods for using UV spectral information to more reliably predict  $H\beta$ -based line widths and black hole masses. We employed the ratio of the peak flux of the Si IV+O IV] line at  $1400 \text{ \AA}$  to the peak flux of C IV as an indicator of the optical EV1, as measured by the equivalent width ratio of [O III] to Fe II, and showed

that adding this UV EV1 indicator to a measure of C IV line width predicts the H  $\beta$  line width with increased accuracy.

We also investigated whether the EV1 dependence persists when line width is calculated using the line dispersion rather than FWHM. It does, but the effect is much less significant. Predicting the H  $\beta$ -based line width and mass using line dispersion and UV spectral measurements provides only a minimal improvement to using a C IV-only prescription.

Including UV EV1 when calculating black hole mass from UV spectra increases agreement between C IV and H  $\beta$ -based black hole mass estimates, reducing the scatter between the two from 0.43 dex to 0.33 dex. Using this prescription, black hole masses can be more reliably calculated from the C IV line using FWHM which is robust to low S/N data.

## ACKNOWLEDGMENTS

J. Runnoe would like to thank Kelly Denney for helpful discussions during the preparation of this work. Z. Shang acknowledges support by the National Natural Science Foundation of China through Grant No. 10773006 and Tianjin Distinguished Professor Funds. We thank the anonymous referee for suggestions that improved this work.

## REFERENCES

- Assef R. J. et al., 2011, *ApJ*, 742, 93  
 Bachev R., Marziani P., Sulentic J. W., Zamanov R., Calvani M., Dultzin Hacyan D., 2004, *ApJ*, 617, 171  
 Baskin A., Laor A., 2005, *MNRAS*, 356, 1029  
 Bentz M. C. et al., 2009, *ApJ*, 705, 199  
 Boroson T. A., 2002, *ApJ*, 565, 78  
 Boroson T. A., Green R. F., 1992, *ApJ*, 80, 109  
 Brotherton M. S., Francis P. J., 1999, in *Astronomical Society of the Pacific Conference Series*, Vol. 162, *Quasars and Cosmology*, Ferland G., Baldwin J., eds., p. 395  
 Brotherton M. S., Wills B. J., Francis P. J., Steidel C. C., 1994, *ApJ*, 430, 495  
 Denney K. D., 2012, *ApJ*, 759, 44  
 Denney K. D., Peterson B. M., Dietrich M., Vestergaard M., Bentz M. C., 2009, *ApJ*, 692, 246  
 Denney K. D., Pogge R. W., Assef R. J., Kochanek C. S., Peterson B. M., Vestergaard M., 2013, *ArXiv e-prints*  
 DiPompeo M. A., Brotherton M. S., Cales S. L., Runnoe J. C., 2012, *MNRAS*, 427, 1135  
 Ho L. C., Goldoni P., Dong X.-B., Greene J. E., Ponti G., 2012, *ApJ*, 754, 11  
 Isobe T., Feigelson E. D., Akritas M. G., Babu G. J., 1990, *ApJ*, 364, 104  
 Kaspi S., Smith P. S., Netzer H., Maoz D., Jannuzi B. T., Giveon U., 2000, *ApJ*, 533, 631  
 Kriss G., 1994, *Astronomical Data Analysis Software and Systems*, 3, 437  
 Laor A., Bahcall J. N., Jannuzi B. T., Schneider D. P., Green R. F., Hartig G. F., 1994a, *ApJ*, 420, 110  
 Laor A., Fiore F., Elvis M., Wilkes B. J., McDowell J. C., 1994b, *ApJ*, 435, 611  
 Laor A., Fiore F., Elvis M., Wilkes B. J., McDowell J. C., 1997, *ApJ*, 477, 93  
 Park D., Woo J.-H., Denney K., Shin J., 2013, *ArXiv e-prints*  
 Peterson B. M. et al., 2005, *ApJ*, 632, 799  
 Peterson B. M. et al., 2004, *ApJ*, 613, 682  
 Peterson B. M., Wanders I., Horne K., Collier S., Alexander T., Kaspi S., Maoz D., 1998, *PASP*, 110, 660  
 Richards G. T., Vanden Berk D. E., Reichard T. A., Hall P. B., Schneider D. P., SubbaRao M., Thakar A. R., York D. G., 2002, *AJ*, 124, 1  
 Runnoe J. C., Brotherton M. S., Shang Z., 2012, *MNRAS*, 422, 478  
 Shang Z. et al., 2011, *ApJS*, 196, 2  
 Shang Z., Wills B. J., Robinson E. L., Wills D., Laor A., Xie B., Yuan J., 2003, *ApJ*, 586, 52  
 Shang Z., Wills B. J., Wills D., Brotherton M. S., 2007, *ApJ*, 134, 294  
 Shen Y., 2013, *ArXiv e-prints*  
 Shen Y., Liu X., 2012, *ApJ*, 753, 125  
 Shen Y. et al., 2011, *ApJS*, 194, 45  
 Sulentic J. W., Bachev R., Marziani P., Negrete C. A., Dultzin D., 2007, *ApJ*, 666, 757  
 Tang B., Shang Z., Gu Q., Brotherton M. S., Runnoe J. C., 2012, *ApJS*, 201, 38  
 Trakhtenbrot B., Netzer H., 2012, *MNRAS*, 427, 3081  
 Vestergaard M., 2002, *ApJ*, 571, 733  
 Vestergaard M., Peterson B. M., 2006, *ApJ*, 641, 689  
 Wills B. J., Brotherton M. S., Fang D., Steidel C. C., Sargent W. L. W., 1993a, *ApJ*, 415, 563  
 Wills B. J., Browne I. W. A., 1986, *ApJ*, 302, 56  
 Wills B. J., Netzer H., Brotherton M. S., Han M., Wills D., Baldwin J. A., Ferland G. J., Browne I. W. A., 1993b, *ApJ*, 410, 534  
 Yuan M. J., Wills B. J., 2003, *ApJL*, 593, L11